MATERIALS CHEMISTRY FRONTIERS

RESEARCH ARTICLE

View Article Online
View Journal | View Issue

Cite this: *Mater. Chem. Front.*, 2023, **7**, 1423

Efficient and stable hybrid conjugated polymer/perovskite quantum dot solar cells†

Hehe Huang,[ab] Xuliang Zhang,[ac] Chenyu Zhao[ab] and Jianyu Yuan *[ab]

Received 5th January 2023,
Accepted 9th February 2023

DOI: 10.1039/d3qm00015j

rsc.li/frontiers-materials

Emerging lead halide perovskite quantum dots (QDs) have attracted great research interest relative to conventional metal chalcogenide-based QDs for applications like solar cells. Meanwhile, such a new type of solution-processable inorganic QD also provides an additional platform to design high performance organic–inorganic hybrid films to maximize their device performance. Herein, we report a hybrid strategy utilizing conjugated polyelectrolyte PFN-Br and all-inorganic $CsPbI_3$ perovskite QDs. There is an urgency to further improve the electronic coupling as well as the ambient stability of $CsPbI_3$ QDs. Using the hybrid strategy, we demonstrated that the hydrophobic PFN-Br can well passivate the $CsPbI_3$ QD surface to reduce defect states as well as suppress the migration of halide ions for better stability. Consequently, the hybrid PFN-Br/$CsPbI_3$ QD solar cell delivers a champion efficiency of 15.07%, outperforming that of 13.31% in the pristine $CsPbI_3$ QD based one. Moreover, the hybrid blend film exhibits significantly improved storage stability under ambient conditions. We believe that these results would provide a new design principle for hybrid organic–inorganic systems for high-performance optoelectronic devices.

1. Introduction

Lead-halide perovskite quantum dots (QDs) have attracted intense interest in photovoltaic applications due to their great flexibility in composition, tunable bandgap, multiple exciton effect and ambient solution-processing.[1–3] Due to their more suitable optical bandgap (1.73 eV), all-inorganic $CsPbI_3$ QDs are considered the most promising light absorbing materials in the QD family for application in the next-generation photovoltaic devices.[4–7] Besides, the $CsPbI_3$ bulk perovskite has a high phase transition temperature of 320 °C to the desired cubic phase, while it tends to transform into a less conductive orthorhombic phase (2.82 eV) at room temperature.[8] In contrast, $CsPbI_3$ QDs can solve the critical phase stability issue and stabilize the cubic phase at room temperature with precise control over the solution-to-film crystallization process. Since the first report in 2016, $CsPbI_3$ QD solar cells have exhibited rapidly improved power conversion efficiency (PCE), surpassing all other colloidal QDs when a certified device efficiency of 13.4% was reported in 2017, and now the PCE has been significantly improved over 16% with growing progress in surface passivation and device architecture engineering.[8–11]

Although these emerging $CsPbI_3$ QDs display superior optoelectronic properties as well as great potential in energy conversion applications, there is still a fundamental requirement for further improving the electronic coupling as well as the stability of these QD solar cells.[12–14] In general, the as-synthesized $CsPbI_3$ QDs are usually capped with long-chain surface ligands to guarantee good passivation as well as good dispersion in solvents, such as oleic acid (OA) and oleylamine (OAm). However, their insulating and dynamic nature is detrimental to carrier transport and stability. Lots of efforts have been dedicated to exchange these long-chain ligands with short conductive ligands during purification or the solid-state post-treatment process.[15–18] Under these circumstances, if these long-chain ligands are excessively exchanged or the surface trap states are inefficiently passivated, increased surface defect density as well as the stability issue will hinder the photovoltaic performance. In comparison with currently reported short ligands, conjugated polymers usually bear various functional side-groups that could efficiently passivate the defects, and the hydrophobic backbone would provide a physical barrier to prevent moisture from penetrating the QDs.[19,20] Hybrid polymer/metal chalcogenide-based QDs have been intensively investigated, but their efficiency is relatively low below 10%.[21–23] Considering the higher efficiency in $CsPbI_3$ QD solar cells, the hybrid polymer/$CsPbI_3$ QD strategy is promising for further enhancing the electronic coupling and stability.

[a] *Institute of Functional Nano & Soft Materials (FUNSOM), Soochow University, Suzhou, Jiangsu 215123, P. R. China. E-mail: jyyuan@suda.edu.cn*
[b] *Jiangsu Key Laboratory of Advanced Negative Carbon Technologies, Soochow University, Suzhou, 215123, Jiangsu, P. R. China*
[c] *Jiangsu Key Laboratory for Carbon-Based Functional Materials and Devices, Soochow University, Suzhou, Jiangsu 215123, P. R. China*

† Electronic supplementary information (ESI) available. See DOI: https://doi.org/10.1039/d3qm00015j

In this work, inspired by the hybrid concept, we employed a widely adopted cationic conjugated polyelectrolyte poly [(9,9-bis(3′-((*N*,*N*-dimethyl)-*N*-ethylammonium)-propyl)-2,7-fluorene)-*alt*-2,7-(9,9-dioctylfluorene)] dibromide (PFN-Br) to passivate and improve the stability of $CsPbI_3$ QDs. The lone pairs on the nitrogen of quaternary ammonium undergo positive charge transport between neighbouring QDs and possess the ability to reduce the defect density in QD arrays without sacrificing electrical conductivity. On the other hand, bromide anions could increase the lattice micro-strain to suppress the migration of halide ions to further improve the stability. Using this strategy, the hybrid PFN-Br/$CsPbI_3$ QD device exhibits a champion efficiency of 15.07% with an enhanced voltage (V_{oc}) and short circuit current density (J_{sc}), which is enhanced relative to the pristine QD based one (13.31%). More importantly, the hybrid PFN-Br/QD blend film exhibits significantly improved storage stability under ambient conditions.

2. Experimental

2.1 Preparation of PFN-Br/$CsPbI_3$ QD hybrid solution

After one day of self-purification in a refrigerator, the as-synthesized $CsPbI_3$ QD solution was centrifuged for five minutes at a speed of 4000 rpm. The collected supernatant was split into two vials: one served as the control $CsPbI_3$ QDs, while the other was utilized as the hybrid PFN-Br/$CsPbI_3$ QD sample by directly adding a small portion of PFN-Br powder into the solution. After stirring in a glovebox for 10 min, the PFN-Br/$CsPbI_3$ QD hybrid solution was centrifuged again at a speed of 4000 rpm to remove the excess PFN-Br powder. For further solar cell fabrication, both samples needed to be concentrated to 70 mg mL^{-1} in *n*-octane solution.

2.2 Preparation of solar cell devices

The etched FTO glass substrates were ultrasonically washed with deionized water, isopropyl alcohol, and acetone for 15 min, respectively. Then, the substrates were dried under N_2 flow and treated with ultraviolet ozone for 30 minutes. The TiO_2 electron transfer layer was then deposited through a previously reported chemical bath deposition method.[24] Subsequently, the TiO_2 film was annealed at 200 °C for 30 min and treated with ultraviolet ozone for 15 minutes. After that, the QD films were deposited through a layer-by-layer spin-coating process. The $CsPbI_3$ QD or PFN-Br/$CsPbI_3$ QD hybrid solution was spin-coated onto the top of the TiO_2 film at 1000 rpm for 15 s and 2000 rpm for 20 s in an air glove box with controlled humidity lower than 15%. Then, 150 μL of MeOAc was dropwise added onto the $CsPbI_3$ QD array for 5 s and spun at 2000 rpm for 20 s. The above process was repeated 5 times to obtain the desired thickness of the QD film. Afterward, the as-cast QD film was quickly dipped into a FAI saturated solution in ethyl acetate for 3 s followed by rinsing with neat MeOAc. Then, the prepared QD film was transferred into the N_2 glovebox and annealed at 70 °C for 10 min. The hole transport layer was spin coated at 3000 rpm for 40 s using a PTAA solution. The PTAA solution was prepared by dissolving PTAA powder in toluene at a concentration of 30 mg/mL, followed by doping an equal volume of 1.5 mg mL^{-1} tris(pentafluorophenyl)-borane toluene solution. Finally, MoO_3 (8 nm) and Ag (120 nm) were deposited by thermal evaporation under a vacuum of 2×10^{-6} mbar.

3. Results and discussion

The $CsPbI_3$ QDs capped with OA and OAm ligands were synthesized and purified using a previously reported method.[8,25] The chemical structure of PFN-Br is illustrated in Fig. 1a. The preparation of the PFN-Br/$CsPbI_3$ QD hybrid solutions is shown in Fig. 1b with details described in the Experimental section. In general, the PFN-Br powder was directly added into the $CsPbI_3$ QD solution and further stirred for 10 minutes. To explore the surface chemistry of $CsPbI_3$ QDs after PFN-Br modification, Fourier transform infrared spectroscopy (FTIR) and X-ray photoelectron spectroscopy (XPS) were performed. As shown in Fig. S1 (ESI†), the signals at 2768–2985 cm^{-1} were mainly assigned to the typical stretching model of C–H_x that derived from the oleyl groups on OA and OAm ligands.[26] The hybrid PFN-Br/$CsPbI_3$ QDs exhibit a lower C–H_x peak intensity relative to the control sample, demonstrating that the surface long chain OA/OAm ligands were partly removed when blending with PFN-Br. In addition, as shown in Fig. 1c, the characteristic signal at 815 cm^{-1} in the hybrid film is ascribed to the aromatic C–H bending of PFN-Br, indicating that the PFN-Br was successfully attached to the $CsPbI_3$ QD surface.[27,28] To further gain insight into the interaction between PFN-Br and $CsPbI_3$ QDs, the XPS measurement was carried out. Fig. 1d and e show the Pb 4f and I 3d core-level spectra, respectively. In short, all characteristic peaks shift toward higher binding energy position in both Pb 4f (0.2 eV) and I 3d (0.2 eV) core-level spectra after blending with PFN-Br, suggesting the change of the chemical environment as well as the interaction between the PFN-Br and Pb^{2+} and I^-.[29] In contrast, we observe a negligible peak position shift in the core level of Cs 3d after introducing PFN-Br (Fig. S2, ESI†), suggesting less chemical interaction between PFN-Br and Cs^+ cations. Besides, the I/Pb ratio was further calculated based on the XPS results, and the PFN-Br/$CsPbI_3$ QD hybrid sample exhibits a higher I/Pb ratio of 4.22 relative to that of 3.84 in the control one. The halide-enrichment on the QD surface after PFN-Br modification implies the decrease of I vacancies, which is beneficial for suppressing non-radiative recombination.[30] In addition, the content of Br in $CsPbI_3$ QDs could increase the lattice micro-strain to suppress the migration of halide ions to further increase the I content in the treated QD films. All of these above results suggest that the native surface capping ligands were partially substituted by PFN-Br (as illustrated in Fig. 1b), and the PFN-Br ligand could chemically bind to the $CsPbI_3$ QD surface to achieve desired surface passivation.

Transmission electron microscopy (TEM) measurements were further carried out to verify the effect of PFN-Br addition on the $CsPbI_3$ QD morphology. Fig. 2a shows the TEM image of

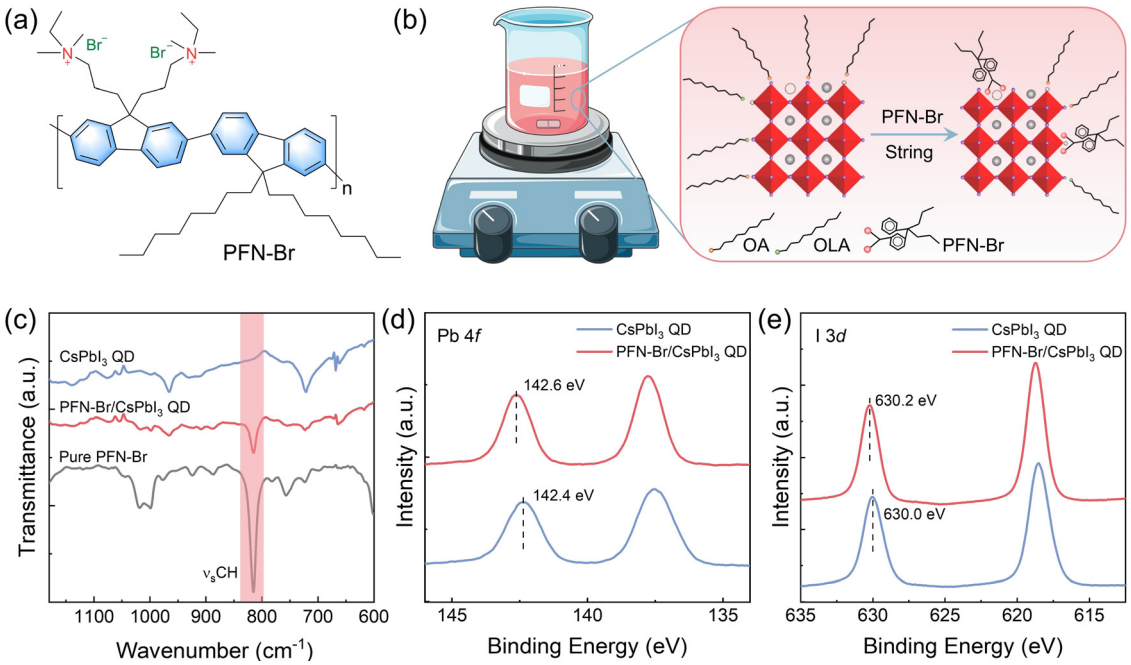

Fig. 1 (a) Chemical structure of PFN-Br. (b) Schematic diagram of the preparation of the PFN-Br/$CsPbI_3$ QD hybrid solution. (c) FTIR spectra of $CsPbI_3$ QD, PFN-Br and PFN-Br/$CsPbI_3$ QD hybrids. (d) Pb 4f and (e) I 3d XPS core level spectra of $CsPbI_3$ QD and PFN-Br/$CsPbI_3$ QD hybrids.

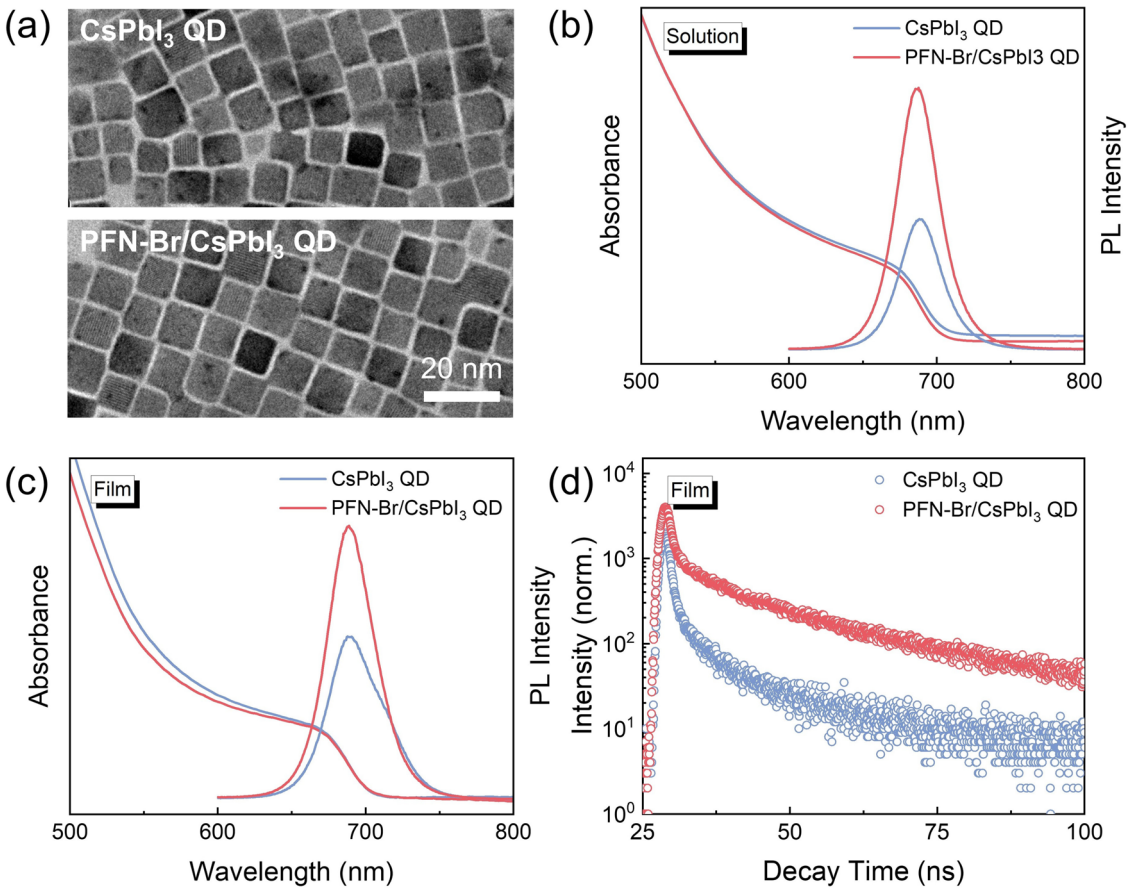

Fig. 2 (a) TEM image of $CsPbI_3$ QD and PFN-Br/$CsPbI_3$ QD samples. (b) and (c) UV-vis absorption and steady-state PL spectra of $CsPbI_3$ QD and hybrid PFN-Br/$CsPbI_3$ QD systems (solutions and films). (d) TRPL spectra of $CsPbI_3$ QD and PFN-Br/$CsPbI_3$QD hybrid films.

the control $CsPbI_3$ QD and PFN-Br/$CsPbI_3$QD hybrid films from which it can be seen that both samples display the same nanocube morphology with similar average sizes, as confirmed by the size distribution statistics (Fig. S3, ESI†). These results indicate that the PFN-Br addition has a negligible effect on the $CsPbI_3$ QD morphology and size distribution. In addition, the high-resolution TEM images of both the control and PFN-Br/$CsPbI_3$ QD hybrid samples have a lattice spacing of 6.25 Å and 6.16 Å (as shown in Fig. S4, ESI†), respectively, corresponding to the (100) crystal facet of the cubic structure, suggesting that the introduction of PFN-Br would lead to the lattice contraction of $CsPbI_3$ QDs. Such a conclusion was further confirmed by X-ray diffraction (XRD) characterization (Fig. S5, ESI†). The XRD patterns of both samples can be indexed to cubic $CsPbI_3$ with no changes in the crystalline phase by adding PFN-Br. Meanwhile, UV-vis absorption and steady-state photoluminescence (PL) spectroscopies were performed to determine the effect of PFN-Br on the optical properties. As shown in Fig. 2b, in comparison with control $CsPbI_3$ QD solution, the PFN-Br/$CsPbI_3$ QD hybrid solution exhibits a slight blue shift, and the PL emission peak intensity significantly increases after adding PFN-Br. Such a blue shift and increased PL intensity could be considered as a result of the defect passivation and reduced non-radiative recombination. For the $CsPbI_3$ QD solid state film (Fig. 2c), the UV-vis absorption and steady-state PL spectra display the same trend when compared to QD solution, indicating lower trap state intensity in the PFN-Br/$CsPbI_3$ QD hybrid film. Moreover, the time-resolved PL (TRPL) spectra (Fig. 2d) were obtained for both films to further investigate the change of defect states, and the detailed parameters of the TRPL spectra extracted by bi-exponential fitting are summarized in Table S1(ESI†). Apparently, the hybrid PFN-Br/$CsPbI_3$ QD film exhibits a longer PL lifetime of 5.31 ns relative to that of 1.68 ns in the control film, which indicates that the PFN-Br based hybrid strategy could effectively passivate the $CsPbI_3$ QDs.

After gathering all of the above results, it could be inferred that PFN-Br could partially remove the surface long-chain ligands and well passivate the QD surface through molecular interactions. However, for application in optoelectronic devices, the properties of QD films are crucial for the resultant device performance. Therefore, we performed a set of characterization techniques on the QD solid films to gain insight into the QD film structure as well as the dynamics of photoinduced charges. As shown in Fig. 3a, we observe lots of pin-holes in the top-view scanning electron microscopy (SEM) image of the control $CsPbI_3$ QD film, and it displays loosely stacked QD microstructures. In contrast, the PFN-Br/$CsPbI_3$ QD hybrid film exhibits smooth and compact surface morphology with reduced pinholes (Fig. 3b). Furthermore, the compositional elements Cs, Pb, I and Br of PFN-Br/$CsPbI_3$ QD films were homogeneously distributed, as seen by the corresponding SEM elemental mapping images in Fig. S6 (ESI†). To further verify the passivation and improved uniformity in the hybrid QD films, two-dimensional (2D) PL mapping characterization was carried out (Fig. 3c and d). In comparison with the control $CsPbI_3$ QD film, the PFN-Br/$CsPbI_3$ QD hybrid film exhibits significantly higher PL intensity, which is consistent with the steady-state PL spectra. Meanwhile, a more homogenous PL intensity was observed in the PFN-Br/QD film relative to the control one,

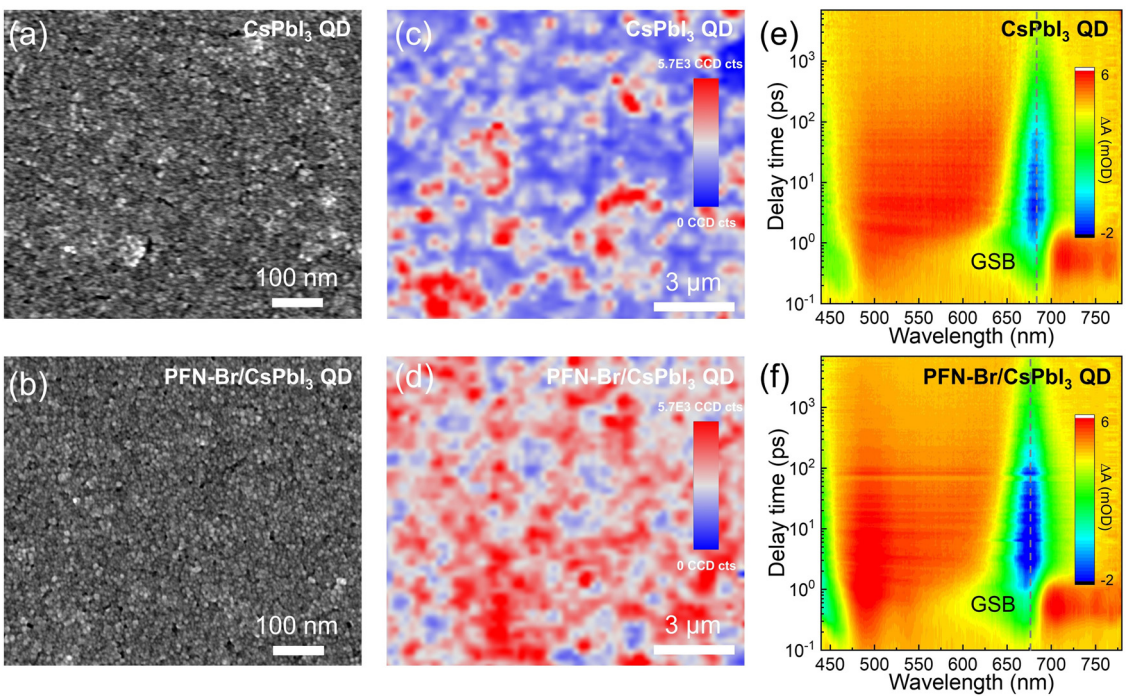

Fig. 3 Top-view SEM images of the (a) $CsPbI_3$ and (b) PFN-Br/$CsPbI_3$ QD hybrid films, respectively. PL mapping of the (c) $CsPbI_3$ and (d) PFN-Br/$CsPbI_3$ QD films, respectively. Pseudo-color TA map of the (e) $CsPbI_3$ and (f) PFN-Br/$CsPbI_3$ QD hybrid films, respectively.

indicating that PFN-Br could shield the QDs and result in the enhanced film uniformity. Furthermore, femtosecond transient absorption (fs-TA) spectroscopy was performed to demonstrate the relationship between the $CsPbI_3$ QD film morphology and the carrier dynamics. Fig. 3e and f depict the pseudo-color TA plot of control $CsPbI_3$ and hybrid PFN-Br/$CsPbI_3$ QD films, and the ground-state bleach (GSB) is found at 682 nm for the control film and 674 nm for the hybrid PFN-Br/QD film, respectively. The GSB decay dynamics of both films were fitted by the tri-exponential fitting (Fig. S7 and Table S2, ESI†), where the three time-resolved components of τ_1, τ_2, and τ_3 corresponding to the timescale of hot-phonon bottleneck, Auger recombination, and charge transfer, respectively.[31,32] Compared to the control film (τ_1 = 106.7 ps, τ_2 = 438.7 ps, and τ_3 = 1354.5 ps), the PFN-Br/$CsPbI_3$ QD hybrid film shows an overall longer constant (τ_1 = 164.4 ps, τ_2 = 473.2 ps, and τ_3 = 2993.1 ps). The prolonged Auger recombination and charge transfer all indicate that PFN-Br can lower the surface trap states and stimulate the carrier charge transfer in the solid-state film, which is beneficial for achieving better device performance when applied in solar cells.

Finally, to investigate the photovoltaic performance of the hybrid PFN-Br/$CsPbI_3$ QD blend, a solar cell with a planar architecture of glass/FTO/TiO_2 (40 nm)/$CsPbI_3$ QDs (~400 nm)/PTAA (70 nm)/MoO_3 (8 nm)/Ag (120 nm) was fabricated. As shown in Fig. 4a, each layer of the solar cell device could be clearly identified from the cross-sectional SEM image. Fig. 4b shows the current density–voltage (J–V) curves of $CsPbI_3$ QD devices measured under AM 1.5G solar illumination at 100 mW cm^{-2}, with the detailed device parameters summarized in Table S3 (ESI†). It can be seen that the hybrid PFN-Br/$CsPbI_3$ QD device delivered a champion PCE of 15.07% with an enhanced open-circuit voltage (V_{oc}) of 1.251 V, a short-circuit current density (J_{sc}) of 16.22 mA cm^{-2} and a fill factor (FF) of 0.74, which outperforms that of the pristine $CsPbI_3$ QD device (13.31%). The enhanced PCE of the PFN-Br/$CsPbI_3$ QD device was mainly attributed to the improved J_{sc} and V_{oc} caused by the enhanced charge transport, increase of band gap by the doping

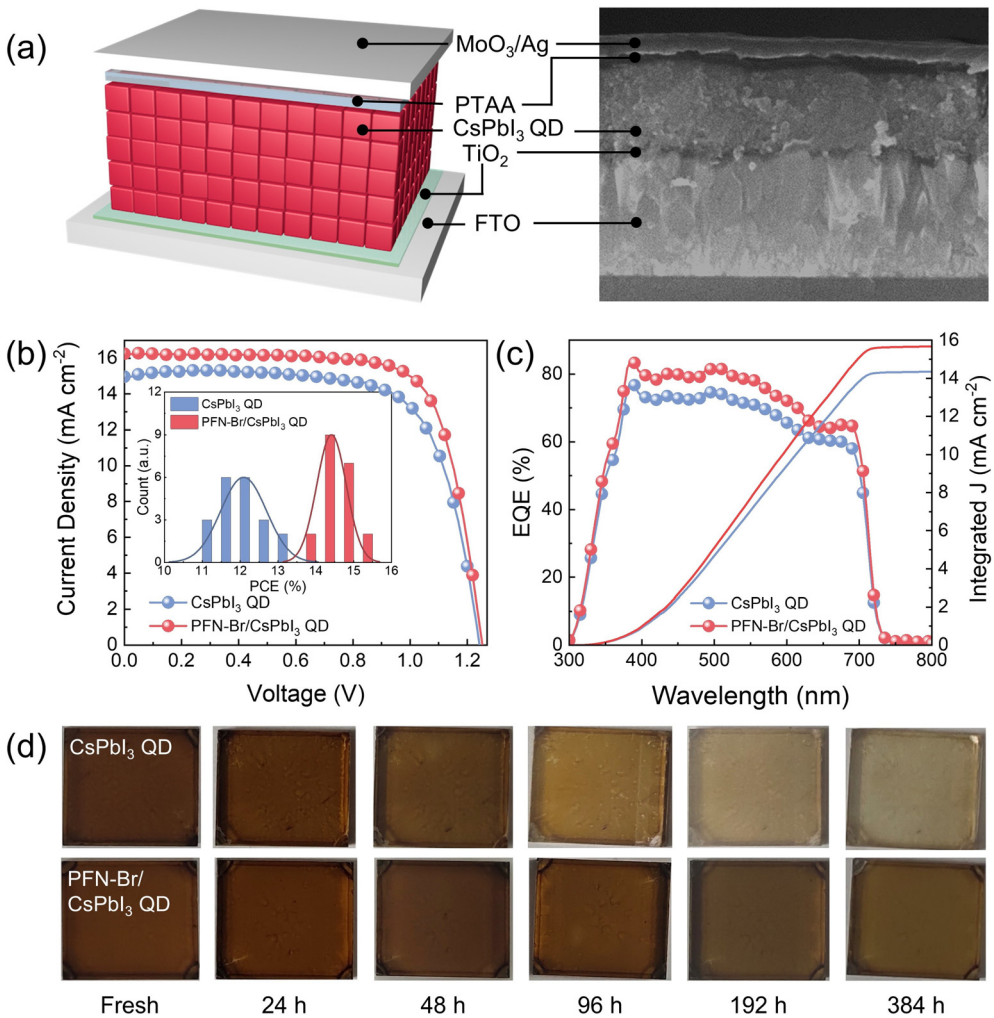

Fig. 4 (a) The device structure and cross-sectional SEM image of the solar cell device. (b) J–V curves of $CsPbI_3$ QD and PFN-Br/$CsPbI_3$ QD solar cells. The inset shows the PCE distribution histograms of 20 devices. (c) EQE spectra with integrated photocurrent density of $CsPbI_3$ QD and PFN-Br/$CsPbI_3$ QD devices. (d) Photographs of $CsPbI_3$ QD and PFN-Br/$CsPbI_3$ QD films stored under ambient conditions (20–25 °C and relative humidity: 30–40%).

of Br^- and defect passivation effect. To further verify the reproducibility of the device performance, 20 individual cells were collected (inset in Fig. 4b). According to the results, the hybrid PFN-Br/$CsPbI_3$ QD solar cells exhibit decent repeatability and higher average PCE values relative to the control $CsPbI_3$ QD based one. Meanwhile, the external quantum efficiency (EQE) characterization was performed on the optimized device with the spectra shown in Fig. 4c. We observe that the hybrid PFN-Br/$CsPbI_3$ QD device exhibits a higher EQE value over the whole photo-response area, suggesting enhanced carrier dissociation and extraction efficiency. The integrated J_{sc} values from the EQE spectra are 14.35 and 15.68 mA cm^{-2} for the control and PFN-Br $CsPbI_3$ QD devices, respectively, which is consistent with the J_{sc} obtained from the *J–V* measurement. Furthermore, to assess the change in the energy band structure, the energy levels of the active layer were characterized by ultraviolet photoelectron spectroscopy (UPS) with the corresponding optical bandgap energies (Fig. S8 and S9, ESI†). The PFN-Br/$CsPbI_3$ QD hybrid film exhibits a graded conduction band (CB) and valence band (VB) relative to the control $CsPbI_3$ QD film, which is advantageous for effective charge carrier extraction and decreasing carrier recombination loss.[33,34] To further understand the enhancement of stability, as shown in Fig. 4d, the $CsPbI_3$ QD film was stored and captured under ambient conditions (20–25 °C, and relative humidity: 30–40%). The color of the pristine $CsPbI_3$ QD film gradually changes after 48 hours of storage. In contrast, after 384 hours of storage, the PFN-Br/$CsPbI_3$ QD hybrid film maintains almost its initial brown color with relatively slow degradation, suggesting that the protection of PFN-Br could slow down the phase transition of cubic $CsPbI_3$ QDs. Overall, these significant findings demonstrate that the enhanced charge carrier dynamic process from effective surface passivation contributes to the improved photovoltaic performance and stability of the PFN-Br/$CsPbI_3$ QD hybrid blend.

4. Conclusions

In conclusion, we have demonstrated an effective organic conjugated polymer/perovskite QD hybrid system using a cationic conjugated polyelectrolyte PFN-Br and emerging $CsPbI_3$ QDs. A high PCE of 15.07% has been achieved for hybrid solar cells, and is greatly enhanced relative to the control pristine $CsPbI_3$ QD based devices (13.31%). We thoroughly investigated the addition of PFN-Br into $CsPbI_3$ QDs and confirmed that PFN-Br can partially remove the surface long-chain ligands and well passivate the $CsPbI_3$ QDs. The passivation is beneficial for improving the charge transfer and carrier extraction in the hybrid film, as well as suppressing the migration of halide ions to achieve better stability. We believe that these results provide a simple yet effective strategy to develop efficient organic/QD hybrid films and could further boost the efficiencies of QD based solar cells.

Conflicts of interest

The authors declare that they have no known competing financial interests.

Acknowledgements

This work was financially supported by the National Key Research and Development Program of China (No. 2019YFE0108600), the National Natural Science Foundation of China (No. 52261145696 and 52073198), the China Postdoctoral Science Foundation (Grant No. 2021T140495), the Natural Science Foundation of Jiangsu Province (BK20211598), the Science and Technology Program of Suzhou (ST202219), and the "111" project, Collaborative Innovation Center of Suzhou Nano Science and Technology, Soochow University.

References

1 F. P. Garcia de Arquer, D. V. Talapin, V. I. Klimov, Y. Arakawa, M. Bayer and E. H. Sargent, Semiconductor quantum dots: Technological progress and future challenges, *Science*, 2021, **373**, eaaz8541.
2 J. Yuan, A. Hazarika, Q. Zhao, X. Ling, T. Moot, W. Ma and J. M. Luther, Metal Halide Perovskites in Quantum Dot Solar Cells: Progress and Prospects, *Joule*, 2020, **4**, 1160–1185.
3 J. J. Yoo, G. Seo, M. R. Chua, T. G. Park, Y. Lu, F. Rotermund, Y.-K. Kim, C. S. Moon, N. J. Jeon, J.-P. Correa-Baena, V. Bulovic, S. S. Shin, M. G. Bawendi and J. Seo, Efficient perovskite solar cells via improved carrier management, *Nature*, 2021, **590**, 587–593.
4 X. Ling, J. Yuan and W. Ma, The Rise of Colloidal Lead Halide Perovskite Quantum Dot Solar Cells, *Acc. Mater. Res.*, 2022, **3**, 866–878.
5 Y. Wang, M. I. Dar, L. K. Ono, T. Zhang, M. Kan, Y. Li, L. Zhang, X. Wang, Y. Yang, X. Gao, Y. Qi, M. Grätzel and Y. Zhao, Thermodynamically stabilized β-$CsPbI_3$–based perovskite solar cells with efficiencies >18%, *Science*, 2019, **365**, 591–595.
6 X. Zhang, H. Huang, X. Ling, J. Sun, X. Jiang, Y. Wang, D. Xue, L. Huang, L. Chi, J. Yuan and W. Ma, Homojunction Perovskite Quantum Dot Solar Cells with over 1 μm-Thick Photoactive Layer, *Adv. Mater.*, 2022, **34**, 2105977.
7 J. Jeong, M. Kim, J. Seo, H. Lu, P. Ahlawat, A. Mishra, Y. Yang, M. A. Hope, F. T. Eickemeyer, M. Kim, Y. J. Yoon, I. W. Choi, B. P. Darwich, S. J. Choi, Y. Jo, J. H. Lee, B. Walker, S. M. Zakeeruddin, L. Emsley, U. Rothlisberger, A. Hagfeldt, D. S. Kim, M. Grätzel and J. Y. Kim, Pseudo-halide anion engineering for α-$FAPbI_3$ perovskite solar cells, *Nature*, 2021, **592**, 381–385.
8 A. Swarnkar, A. R. Marshall, E. M. Sanehira, B. D. Chernomordik, D. T. Moore, J. A. Christians, T. Chakrabarti and J. M. Luther, Quantum dot-induced phase stabilization of α-$CsPbI_3$ perovskite for high-efficiency photovoltaics, *Science*, 2016, **354**, 92–95.
9 E. M. Sanehira, A. R. Marshall, J. A. Christians, S. P. Harvey, P. N. Ciesielski, L. M. Wheeler, P. Schulz, L. Y. Lin, M. C. Beard and J. M. Luther, Enhanced mobility $CsPbI_3$ quantum dot arrays for record-efficiency, high-voltage photovoltaic cells, *Sci. Adv.*, 2017, **3**, eaao4204.

10 J. Chen, D. Jia, R. Zhuang, Y. Hua and X. Zhang, Highly Orientated Perovskite Quantum Dot Solids for Efficient Solar Cells, *Adv. Mater.*, 2022, **34**, e2204259.
11 D. Jia, J. Chen, R. Zhuang, Y. Hua and X. Zhang, Inhibiting lattice distortion of $CsPbI_3$ perovskite quantum dots for solar cells with efficiency over 16.6%, *Energy Environ. Sci.*, 2022, **15**, 4201–4212.
12 J. Khan, X. Zhang, J. Yuan, Y. Wang, G. Shi, R. Patterson, J. Shi, X. Ling, L. Hu, T. Wu, S. Dai and W. Ma, Tuning the Surface-Passivating Ligand Anchoring Position Enables Phase Robustness in $CsPbI_3$ Perovskite Quantum Dot Solar Cells, *ACS Energy Lett.*, 2020, **5**, 3322–3329.
13 J. Pan, Y. Shang, J. Yin, M. De Bastiani, W. Peng, I. Dursun, L. Sinatra, A. M. El-Zohry, M. N. Hedhili, A. H. Emwas, O. F. Mohammed, Z. Ning and O. M. Bakr, Bidentate Ligand-Passivated $CsPbI_3$ Perovskite Nanocrystals for Stable Near-Unity Photoluminescence Quantum Yield and Efficient Red Light-Emitting Diodes, *J. Am. Chem. Soc.*, 2018, **140**, 562–565.
14 X. Ling, J. Yuan, X. Zhang, Y. Qian, S. M. Zakeeruddin, B. W. Larson, Q. Zhao, J. Shi, J. Yang, K. Ji, Y. Zhang, Y. Wang, C. Zhang, S. Duhm, J. M. Luther, M. Grätzel and W. Ma, Guanidinium-Assisted Surface Matrix Engineering for Highly Efficient Perovskite Quantum Dot Photovoltaics, *Adv. Mater.*, 2020, **32**, 2001906.
15 Y. K. Wang, F. Yuan, Y. Dong, J. Y. Li, A. Johnston, B. Chen, M. I. Saidaminov, C. Zhou, X. Zheng, Y. Hou, K. Bertens, H. Ebe, D. Ma, Z. Deng, S. Yuan, R. Chen, L. K. Sagar, J. Liu, J. Fan, P. Li, X. Li, Y. Gao, M. K. Fung, Z. H. Lu, O. M. Bakr, L. S. Liao and E. H. Sargent, All-Inorganic Quantum-Dot LEDs Based on a Phase-Stabilized α-$CsPbI_3$ Perovskite, *Angew. Chem., Int. Ed.*, 2021, **60**, 16164–16170.
16 Y. Wang, C. Duan, X. Zhang, J. Sun, X. Ling, J. Shi, L. Hu, Z. Zhou, X. Wu, W. Han, X. Liu, C. Cazorla, D. Chu, S. Huang, T. Wu, J. Yuan and W. Ma, Electroluminescent Solar Cells Based on $CsPbI_3$ Perovskite Quantum Dots, *Adv. Funct. Mater.*, 2021, **32**, 2108615.
17 X. Ling, S. Zhou, J. Yuan, J. Shi, Y. Qian, B. W. Larson, Q. Zhao, C. Qin, F. Li, G. Shi, C. Stewart, J. Hu, X. Zhang, J. M. Luther, S. Duhm and W. Ma, 14.1% $CsPbI_3$ Perovskite Quantum Dot Solar Cells via Cesium Cation Passivation, *Adv. Energy Mater.*, 2019, **9**, 1900721.
18 X. Zhang, H. Huang, Y. M. Maung, J. Yuan and W. Ma, Aromatic amine-assisted pseudo-solution-phase ligand exchange in $CsPbI_3$ perovskite quantum dot solar cells, *Chem. Commun.*, 2021, **57**, 7906–7909.
19 J. Yuan, X. Zhang, J. Sun, R. Patterson, H. Yao, D. Xue, Y. Wang, K. Ji, L. Hu, S. Huang, D. Chu, T. Wu, J. Hou and J. Yuan, Hybrid Perovskite Quantum Dot/Non-Fullerene Molecule Solar Cells with Efficiency Over 15%, *Adv. Funct. Mater.*, 2021, **31**, 2101272.
20 S. Lim, D. H. Lee, H. Choi, Y. Choi, D. G. Lee, S. B. Cho, S. Ko, J. Choi, Y. Kim and T. Park, High-Performance Perovskite Quantum Dot Solar Cells Enabled by Incorporation with Dimensionally Engineered Organic Semiconductor, *Nanomicro Lett.*, 2022, **14**, 204.
21 X. Du, Q. Zeng, G. Jin, F. Liu, T. Ji, Y. Yue, Y. Yang, H. Zhang and B. Yang, Constructing Post-Permeation Method to Fabricate Polymer/Nanocrystals Hybrid Solar Cells with PCE Exceeding 6%, *Small*, 2017, **13**, 1603771.
22 Y. N. Zhang, Y. Y. Kan, K. Gao, M. F. Gu, Y. Shi, X. L. Zhang, Y. Xue, X. N. Zhang, Z. K. Liu, Y. Zhang, J. Y. Yuan, W. L. Ma and A. K. Y. Jen, Hybrid Quantum Dot/Organic Heterojunction: A Route to Improve Open-Circuit Voltage in PbS Colloidal Quantum Dot Solar Cells, *ACS Energy Lett.*, 2020, **5**, 2335–2342.
23 S. W. Baek, S. Jun, B. Kim, A. H. Proppe, O. Ouellette, O. Voznyy, C. Kim, J. Kim, G. Walters, J. H. Song, S. Jeong, H. R. Byun, M. S. Jeong, S. Hoogland, F. P. G. de Arquer, S. O. Kelley, J. Y. Lee and E. H. Sargent, Efficient hybrid colloidal quantum dot/organic solar cells mediated by near-infrared sensitizing small molecules, *Nat. Energy*, 2019, **4**, 969–976.
24 A. Yella, L. P. Heiniger, P. Gao, M. K. Nazeeruddin and M. Grätzel, Nanocrystalline rutile electron extraction layer enables low-temperature solution processed perovskite photovoltaics with 13.7% efficiency, *Nano Lett.*, 2014, **14**, 2591–2596.
25 L. Protesescu, S. Yakunin, M. I. Bodnarchuk, F. Krieg, R. Caputo, C. H. Hendon, R. X. Yang, A. Walsh and M. V. Kovalenko, Nanocrystals of Cesium Lead Halide Perovskites (CsPbX(3), X = Cl, Br, and I): Novel Optoelectronic Materials Showing Bright Emission with Wide Color Gamut, *Nano Lett.*, 2015, **15**, 3692–3696.
26 L. M. Wheeler, E. M. Sanehira, A. R. Marshall, P. Schulz, M. Suri, N. C. Anderson, J. A. Christians, D. Nordlund, D. Sokaras, T. Kroll, S. P. Harvey, J. J. Berry, L. Y. Lin and J. M. Luther, Targeted Ligand-Exchange Chemistry on Cesium Lead Halide Perovskite Quantum Dots for High-Efficiency Photovoltaics, *J. Am. Chem. Soc.*, 2018, **140**, 10504–10513.
27 L. Li, Z. Zhang, C. Ding and J. Xu, Boosting charge separation and photocatalytic CO_2 reduction of $CsPbBr_3$ perovskite quantum dots by hybridizing with P3HT, *Chem. Eng. J.*, 2021, **419**, 129543.
28 F. Carulli, W. Mróz, E. Lassi, C. Sandionigi, B. Squeo, L. Meazza, G. Scavia, S. Luzzati, M. Pasini, U. Giovanella and F. Galeotti, Effect of the introduction of an alcohol-soluble conjugated polyelectrolyte as cathode interlayer in solution-processed organic light-emitting diodes and photovoltaic devices, *Chem. Pap.*, 2018, **72**, 1753–1759.
29 X. Zhang, H. Huang, L. Jin, C. Wen, Q. Zhao, C. Zhao, J. Guo, C. Cheng, H. Wang, L. Zhang, Y. Li, Y. Maung Maung, J. Yuan and W. Ma, Ligand-Assisted Coupling Manipulation for Efficient and Stable FAPbI(3) Colloidal Quantum Dot Solar Cells, *Angew. Chem., Int. Ed.*, 2022, e202214241, DOI: **10.1002/anie.202214241**.
30 C. Bi, Z. Yao, X. Sun, X. Wei, J. Wang and J. Tian, Perovskite Quantum Dots with Ultralow Trap Density by Acid Etching-Driven Ligand Exchange for High Luminance and Stable Pure-Blue Light-Emitting Diodes, *Adv. Mater.*, 2021, **33**, e2006722.
31 A. H. Proppe, J. Xu, R. P. Sabatini, J. Z. Fan, B. Sun, S. Hoogland, S. O. Kelley, O. Voznyy and E. H. Sargent, Picosecond Charge Transfer and Long Carrier Diffusion

Lengths in Colloidal Quantum Dot Solids, *Nano Lett.*, 2018, **18**, 7052–7059.

32 F. Li, S. Zhou, J. Yuan, C. Qin, Y. Yang, J. Shi, X. Ling, Y. Li and W. Ma, Perovskite Quantum Dot Solar Cells with 15.6% Efficiency and Improved Stability Enabled by an α-$CsPbI_3$/$FAPbI_3$ Bilayer Structure, *ACS Energy Lett.*, 2019, **4**, 2571–2578.

33 R. M. Zhao, L. Xie, R. S. Zhuang, T. Wu, R. J. Zhao, L. Q. Wang, L. C. Sun and Y. Hua, Interfacial Defect Passivation and Charge Carrier Management for Efficient Perovskite Solar Cells via a Highly Crystalline Small Molecule, *ACS Energy Lett.*, 2021, **6**, 4209–4219.

34 Q. Jiang, L. Zhang, H. Wang, X. Yang, J. Meng, H. Liu, Z. Yin, J. Wu, X. Zhang and J. You, Enhanced electron extraction using SnO_2 for high-efficiency planar-structure $HC(NH_2)_2PbI_3$-based perovskite solar cells, *Nat. Energy*, 2016, **2**, 16177.

